Proceedings of the Thirty-sixth (2026) International Ocean and Polar Engineering Conference **www.isope.org**
Orlando, Florida, USA, May 31-June 5, 2026

ISBN 978-1-880653-72-2; ISSN 1098-6189

CFD-Based Efficient Optimization Method for the Hydrodynamic Performance of a Flat Merchant Ship

Zhiqiang Liu[a], Xiyang Liu[a], Yanxia Wang [a], Jia Su[a], Decheng Wan[b,]*

[a] Shanghai Branch, China Ship Scientific Research Center, Shanghai, China
[b] Computational Marine Hydrodynamic Lab (CMHL), School of Ocean and Civil Engineering,
Shanghai Jiao Tong University, Shanghai, China
[*]Corresponding author

ABSTRACT

Hull form optimization has been a crucial component in the development of green ship technology. Through hull form optimization, the reduction of ship resistance and the improvement of propulsion efficiency can be achieved. Based on the Free-Form Deformation (FFD) method, this paper couples the dynamic mesh deformation library in the OpenFOAM platform to achieve mesh deformation for a numerical volume mesh. This method can ensure the constant mesh quantity and topological structure of the numerical calculation mesh, serve hull form optimization, and further enhance its efficiency. Taking a flat merchant ship as the research object, this paper optimizes its resistance performance at a speed of 15 knots. The hull stern shape is modified via the volume mesh deformation method based on FFD; Optimal Latin hypercube sampling (OLHS) is adopted for design space sampling, a surrogate model is constructed based on Kriging theory, and a single-objective genetic algorithm is used for optimization iteration. A comprehensive analysis and comparison of the flow fields of the original hull form and the optimized hull form are conducted in this paper. The results show that the apposed volume mesh deformation method operates stably, can effectively achieve smooth deformation of the ship hull form, and improve the efficiency of mesh generation for numerical mesh in hull form optimization. And the resistance reduction of the target hull form is realized through hull form optimization.

KEY WORDS: hull form optimization, FFD, mesh morphing, resistance optimization.

INTRODUCTION

The most time-consuming part in ship form optimization lies in conducting hydrodynamic numerical calculations for different ship forms, so as to obtain their hydrodynamic performance and further establish the relationship between ship form parameters and target hydrodynamic performances. The optimal hull form and the optimized values of target hydrodynamic performance are obtained via optimization algorithms. To reduce the time consumed by numerical calculations and improve the efficiency of hull form optimization, numerous scholars have carried out relevant research from various aspects, which mainly fall into two categories: dimensionality reduction methods and efficient hydrodynamic performance evaluation methods. Dimensionality reduction methods mainly improve the efficiency of ship form optimization by reducing the number of ship forms that need to be calculated, while efficient hydrodynamic performance evaluation methods achieve the same goal by cutting down the time required for numerical simulation.

In terms of design space dimensionality reduction, many scholars use different dimensionality reduction methods in hull form optimization. Taking the resistance optimization of the Wigley hull form as an example, Liu et al. (2021) implemented design space dimensionality reduction by adopting the linear dimensionality reduction method, and presented the specific applications and error analysis of the dimensionality reduction method in preliminary design space dimensionality reduction and subsequent multi-physics field learning for hull form optimization. The results show that the linear dimensionality reduction method can reduce the number of numerical simulation samples required for hull form optimization, thereby decreasing the computational cost of surrogate model-based hull form optimization, and it can be applied to the rapid multi-physics field prediction for any new hull form within the design space. Zhang et al. (2023) adopted a shape optimization method called Principal Component Analysis (PCA) for dimensionality reduction. Taking the KRISO Container Ship (KCS) as the validation model, they carried out the optimization of its bulbous bow. With the aid of PCA, the reconstructed design space achieved an 80% dimensionality reduction with an accuracy of approximately 99%. The results demonstrate that the wave-making resistance of KCS at service speed was reduced by 18%. Liu et al. (2026) carried out research on nonlinear dimensionality reduction based on Deep Neural Networks (DNN), and conducted nonlinear dimensionality reduction optimization for the resistance of the DTMB hull form. Ultimately, this method effectively reduced the number of sample hull form numerical calculations while ensuring the performance of hull form optimization. Serani and Diez (2025) analyzed the application scopes of various dimensionality reduction techniques, covering not only classical linear methods such as PCA, but also more sophisticated nonlinear methods like autoencoders, and even extending to innovative physics-informed driven methods. The research shows that integrating dimensionality reduction methods into the shape optimization framework can effectively alleviate the curse of dimensionality, simplify the calculation process, and optimize the design exploration and performance tuning of complex surfaces.

In terms of efficient hydrodynamic performance evaluation methods, the core approach mainly relies on fast calculation methods or other tools that improve the efficiency of numerical calculations. For instance, ship form optimization based on the potential flow method (Feng et al., 2025; Ji et al., 2025) — compared with viscous flow calculation — features high efficiency and low time consumption, thus effectively reducing the time cost in the numerical calculation. Nazemian et al. (2025) conducted hydrodynamic shape optimization for the DARPA Suboff submarine hull by adopting a discrete adjoint solver integrated with mesh deformation technology in Computational Fluid Dynamics (CFD). The optimization objective was to minimize the total drag. Based on the FFD method, the volume mesh deformation was directly realized during the numerical calculation process, thereby avoiding mesh regeneration. After five optimization iterations, the total drag was reduced by 6.43%. Villa et al. (2021) developed a volume mesh deformation tool based on the FFD method, which achieves volume mesh deformation by combining two tools, namely blockMesh and cfMesh. Taking the calm-water resistance optimization of the DTC hull form as a case study, this tool demonstrated its feasibility and robustness. For all hull forms generated within a relatively large design space, the deformed hull meshes were efficiently and successfully obtained by deforming the initial numerical volume mesh of the initial hull form, without causing mesh inconsistency and quality issues. Combined with the surrogate model method, the calm-water resistance was significantly reduced within a reasonable computational time, with a drag reduction of approximately 10%. Costa et al. (2025) presented the development process of a Proof of Concept (PoC), which is intended to design and optimize hull forms by leveraging Reduced-Order Models (ROMs) — an efficient numerical procedure. These ROMs are derived from processing the CFD field database relevant to the maritime domain, which is established via conducting a Design of Experiments (DOE) study that parameterizes CFD cases using Radial Basis Function (RBF) mesh deformation. Being interactive and suitable for real-time computation, these ROMs yield a maximum percentage error of less than 3.5% in resistance prediction when estimating the resistance of design points outside the original DOE dataset, demonstrating their high predictive accuracy. The resulting ROMs thus lay a solid foundation for the construction of ship digital twins.

Ship form hydrodynamic optimization includes single-objective optimization and multi-objective optimization. Single-objective optimization refers to the optimization carried out for a single ship performance objective that designers prioritize, such as resistance optimization (without considering seakeeping performance) (Park et al., 2015), seakeeping optimization (without considering resistance performance) (Bagheri et al., 2014) , and maneuverability optimization (Kim et al., 2021), etc.

Taking a flat merchant ship as the case study, this paper adopts the volume mesh deformation method based on FFD to construct numerical simulation meshes for different hull forms, thereby reducing the time required for mesh generation and improving the efficiency of hull form optimization. With total drag set as the optimization objective and the underwater stern lines defined as the optimization region, hull form optimization is carried out, along with a comprehensive analysis and comparison of the flow field before and after optimization. The subsequent content is elaborated mainly from two aspects: hull form optimization theory and hull form optimization case application.

HULL FORM OPTIMIZATION THEORY

The surrogate model-based hull form optimization framework is mainly composed of five components: design space sampling, hull deformation, ship performance evaluation, surrogate model construction, and optimization algorithm. The workflow framework is illustrated in Fig. 1.

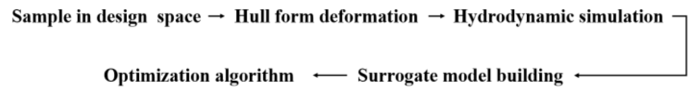

Fig. 1 Simulation-based design framework for hull form optimization

Design Space Sampling: According to the ranges of deformation parameters, sampling is performed within the design space by adopting design of experiments (DOE) sampling methods, such as the OLHS (Miao and Wan, 2020) and SOBOL algorithms (Liu et al., 2017).

Hull Deformation: Based on the sample points sampled in the design space, the original hull form is deformed using a deformation tool to obtain deformed hull forms corresponding to the parameters of different sample points. The deformation method includes FFD, RBF (Jeong and Jeong, 2020), shifting (Wang et al., 2025), and so on.

Hydrodynamic Calculation: After obtaining hull forms, hydrodynamic simulation methods are applied to calculate the hydrodynamic performance of these hull forms, including hull resistance, seakeeping performance, and maneuverability. The simulation software includes OpenFOAM, STAR CCM+, Fluent, and so on.

Surrogate Model Construction: After completing the hydrodynamic performance calculation of all deformed hull forms, the hydrodynamic performance of the sample hull forms corresponding to the deformation parameters can be obtained. A surrogate model is established based on the deformation parameters and their corresponding hydrodynamic performance to characterize the functional mapping relationship between the deformation parameters and the target hydrodynamic performance.

Optimization Algorithm: Based on the constructed surrogate model, an optimization algorithm is used for optimization value search, thereby deriving the theoretical optimal target hydrodynamic values and their corresponding optimal deformation parameters. The optimized hull form is generated by deforming the original hull form with the same deformation tool using the optimal deformation parameters. The target hydrodynamic performance of the optimized hull form is calculated under the same numerical simulation settings, and the results are compared with the theoretical optimal values to verify the optimization effectiveness.

The above is the surrogate model-based hull form optimization framework and its corresponding optimization workflow. It can be seen that this framework involves a wide range of theoretical foundations. This paper mainly introduces the relevant theories adopted herein, such as the FFD method and dynamic mesh deformation technology. For other theories regarding sampling, simulation, and optimization, reference can be made to the corresponding relevant literature (Chang et al., 2023; Dejhalla et al., 2001; Wang et al., 2023).

FFD Theory

The Free-Form Deformation (FFD) method was proposed by Sederberg and Parry et al. in 1986 (Sederberg and Parry, 1986). Its core idea is to embed the geometry within a lattice deformation control volume. When the control points on the lattice deformation control volume are moved, the geometry inside the volume undergoes corresponding deformation, thereby realizing the shape modification of the geometric model. For any arbitrary point $\boldsymbol{X}$, its expression in the local $\boldsymbol{S}-\boldsymbol{T}-\boldsymbol{U}$ coordinate system is given by:

$$\boldsymbol{X} = \boldsymbol{X}_0 + s\boldsymbol{S} + s\boldsymbol{T} + u\boldsymbol{U} \tag{1}$$

Where s, t, and u can be solved by the following formula：

$$s = \frac{\boldsymbol{T}\times\boldsymbol{U}(\boldsymbol{X}-\boldsymbol{X}_0)}{\boldsymbol{T}\times\boldsymbol{U}\cdot\boldsymbol{S}},\ t = \frac{\boldsymbol{S}\times\boldsymbol{U}(\boldsymbol{X}-\boldsymbol{X}_0)}{\boldsymbol{S}\times\boldsymbol{U}\cdot\boldsymbol{T}},\ u = \frac{\boldsymbol{S}\times\boldsymbol{T}(\boldsymbol{X}-\boldsymbol{X}_0)}{\boldsymbol{S}\times\boldsymbol{T}\cdot\boldsymbol{U}} \tag{2}$$

It should be noted that within the lattice control volume, the value ranges of $s, t,$ and u are defined as follows: $0 < s < 1; 0 < t < 1; 0 < u < 1.$ Any control point $\boldsymbol{P}_{ijk}$ on the lattice control volume can be defined such that the lattice is divided into $l+1$ control points along the $\boldsymbol{S}$ direction, $m+1$ along the $\boldsymbol{T}$ direction, and $n+1$ along the $\boldsymbol{U}$ direction. Then, $\boldsymbol{P_{ijk}}$ can be expressed as:

$$\boldsymbol{P_{ijk}} = \boldsymbol{X_0} + \frac{i}{l}\boldsymbol{S} + \frac{j}{m}\boldsymbol{T} + \frac{k}{n}\boldsymbol{U} \tag{3}$$

$\boldsymbol{X_{ffd}}$ denotes the deformed coordinate of an arbitrary point $\boldsymbol{X}$. First, its local coordinates (s, t, u) are calculated using Eq. (2). Then, the deformed coordinate $\boldsymbol{X_{ffd}}$ is obtained via the following Bernstein polynomial formula.

$$\boldsymbol{X_{ffd}} = \sum_{i=0}^{l} \binom{l}{i} (1-s)^{l-i} s^i \sum_{j=0}^{m} \binom{t}{j} (1-t)^{m-j} s^j \sum_{k=0}^{n} \binom{n}{k} (1-u)^{n-k} s^k \boldsymbol{P_{ijk}} \tag{4}$$

Here, $\boldsymbol{X_{ffd}}$ is the vector coordinate in the Cartesian coordinate system, and $\boldsymbol{P_{ijk}}$ is the coordinate of the lattice control point in the Cartesian coordinate system. When the control points $\boldsymbol{P_{ijk}}$ are moved, the new coordinate $\boldsymbol{X_{ffd}}$ of any arbitrary point inside the control volume will be derived accordingly.

Dynamic Mesh Theory

In dynamic meshes (specifically when working with moving/deforming bodies), the integral form of the general transport equation is written as follows:

$$\int_{V_p} \frac{\partial \rho\phi}{\partial t} dV + \int_{V_p} \nabla \cdot [\rho\phi(\boldsymbol{u} - \boldsymbol{u_g})] dV - \int_{V_p} \nabla \cdot [\rho\Gamma_\phi \nabla\phi] dV = \int_{V_p} S_\phi \phi dV \tag{5}$$

Also, the boundary condition of the moving/deforming walls takes into account the mesh velocity. In the FVM, we want to solve the general transport equation for the transported quantity ϕ in a given domain, with given boundary conditions (BC) and initial conditions (IC). As you can see, the only difference with the standard general transport equation is the addition of the mesh velocity. The rest of the FVM formulation remains the same, except for a few considerations related to the moving mesh, as we will see. Notice that the volume dV is a function of time. This implies that the shape of the cells is changing in time, and this might introduce mesh quality problems.

$$\frac{\partial}{\partial t} \int_{V_p} \rho\phi dV = \frac{(\rho\phi V)^{n+1} - (\rho\phi V)^n}{\Delta t} \tag{6}$$

Where n and $n+1$ denote the respective quantities at the current and next time level. Therefore, it is important to choose a time step that does not result in large volume changes between iterations. The $(n+1)$ time level volume V^{n+1} can be computed as follows (volume update),

$$V^{n+1} = V^n + \frac{dV}{dt}\Delta t \tag{7}$$

To satisfy the grid conservation law, the volume time derivative dV/dt of the control volume can be computed as follows,

$$\frac{dV}{dt}\Delta t = \int_{\partial V_p} \boldsymbol{u}_g \cdot d\boldsymbol{S} = \sum_{\boldsymbol{f}} \boldsymbol{u}_{gf} \cdot \boldsymbol{S}_f \tag{8}$$

$$d\boldsymbol{S} = \boldsymbol{n} dS \tag{9}$$

$$\boldsymbol{u}_{gf} \cdot \boldsymbol{S}_f = \frac{\delta V_f}{\Delta t}.$$

To avoid stability and accuracy problems due to cell quality (as the cells are changing in time), the time step should be chosen in such a way that it does not result in large volume changes between iterations.

APPLICATION

This section mainly introduces the application of the volume mesh deformation method in actual hull form optimization. A case study is conducted with the resistance optimization of a flat merchant ship as the research object. The hull model is illustrated in Fig. 2, and the principal dimensions of the hull are presented in Table 1. The sailing speed is set to 15 kn.

Table 1. Principal dimensions of the initial hull

items	hull
L_{pp}/B	5.45
B/T	2.92
C_B	0.7913

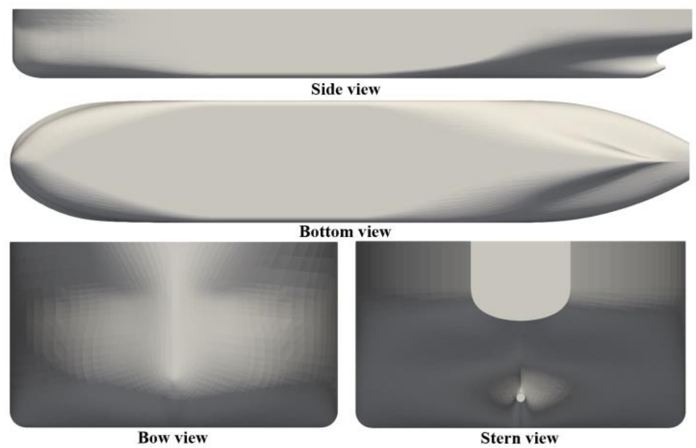

Fig. 2 Hull model

Numerical Precision Verification Of Initial Hull Form

First, the accuracy of numerical calculations is verified. Numerical calculation tools are adopted to compute the resistance of the initial hull, and the results are compared with those of a physical experiment. Eventually, a set of high-precision numerical computational meshes and simulation parameters is obtained. The setup of the numerical computational domain is illustrated in Fig. 3, where the length in the x-direction is 28 m, the height in the z-direction is 15 m, and the width is 10 m. Given the symmetric geometry of the hull, the half-domain modeling approach is employed for mesh generation to reduce the number of computational meshes.

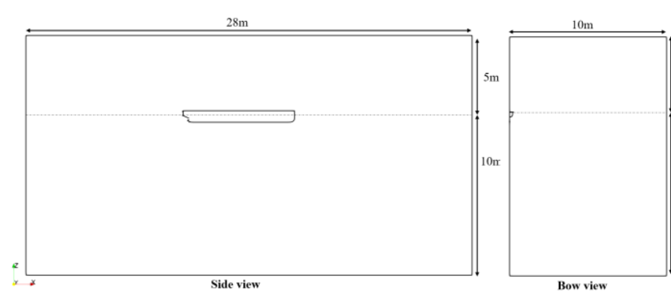

Fig. 3 Computational domain

Mesh generation for the computational domain was performed using blockMesh and snappyHexMesh — the built-in mesh generation tools of OpenFOAM — and the mesh of the computational domain is illustrated in the Fig. 4. To accurately capture wave generation on the free surface, local refinement was applied to the free surface mesh; The free surface and boundary layer meshes are illustrated in the Fig. 5. The hull surface mesh is shown in Fig. 6. The boundary layer thickness was set to 0.0114 m, with an expansion ratio of 1.2 and 5 boundary layer layers. The total number of mesh cells was ultimately 2.03 million. Wall functions were employed to characterize the boundary layer flow.

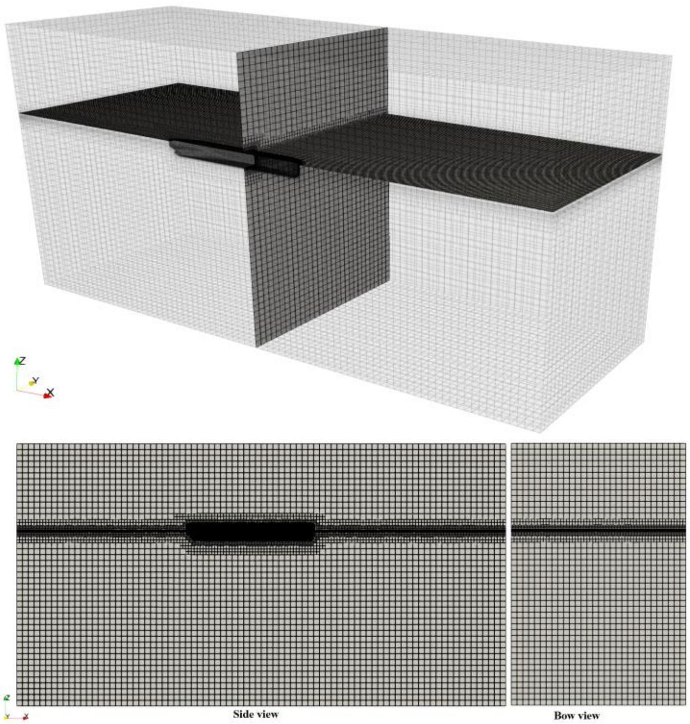

Fig. 4 The computational mesh

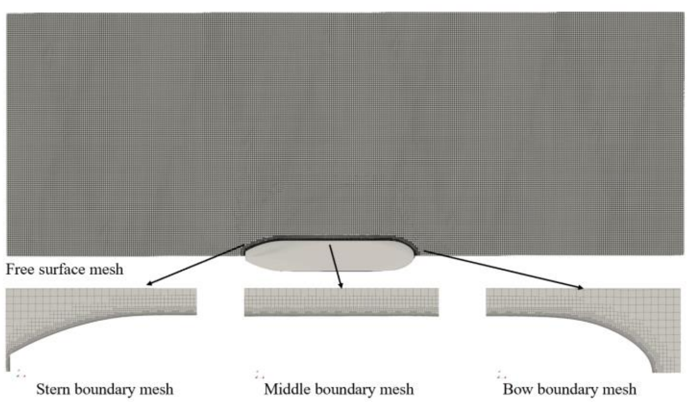

Fig. 5 Free surface mesh and boundary mesh

Fig. 6 Hull surface mesh

Calculations were performed using interFoam — the two-phase incompressible flow solver built into OpenFOAM — with a transient scheme employed for iterative solution. Meanwhile, a hull resistance detection function was configured to monitor and record variations in hull resistance throughout the calculation process. Eventually, a stable flow field around the hull was obtained, and the resistance calculation results, along with the verification outcomes, are presented in Table 2. After verification, the total resistance coefficient derived from numerical calculations was $3.779 * 10^{-3}$, whereas the value obtained from the physical experiment was $3.785 * 10^{-3}$, resulting in a relative error of 0.14%. This demonstrates high computational accuracy, and the relevant CFD parameter settings can be extended to numerical calculations for other hull forms. Because we only have the resistance coefficient, thus , we compare the EFD and CFD for the total resistance coefficient. And in this paper, we focus on using new mesh deformation method to optimize the hull resistance and improving the hull form optimization efficiency. Therefore, we neglected the dynamic sinkage and trim of the hull.

Table 2. The verification of 15kn resistance for the initial hull form

C_t-EFD (10^{-3})	C_t-CFD (10^{-3})	Relative error (%)
3.785	3.779	0.14%

The flow field of the initial hull was visualized for presentation. Fig. 7 depicts the free surface wave pattern of the initial hull, and Fig. 8 shows the relative pressure distribution on the hull surface. The propeller disk wake distribution is presented in Fig. 9 as well. It can be observed from the above flow field figures that the numerical simulation results of the overall flow field are qualitatively consistent with physical laws, with no abnormal flow field phenomena observed. In the region of the propeller disk, the wake is relatively strong near and above the propeller shaft, while the wake intensity is lower in the outer area of the propeller disk.

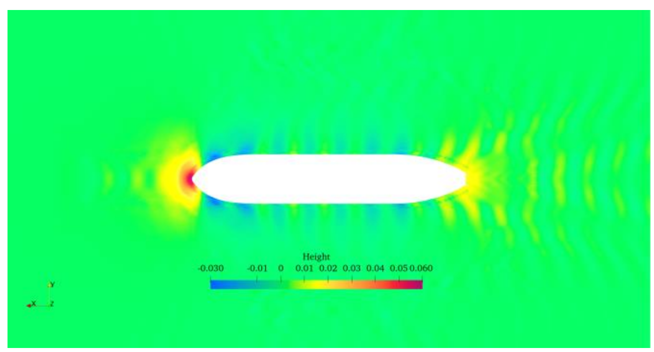

Fig. 7 Free surface of initial hull form

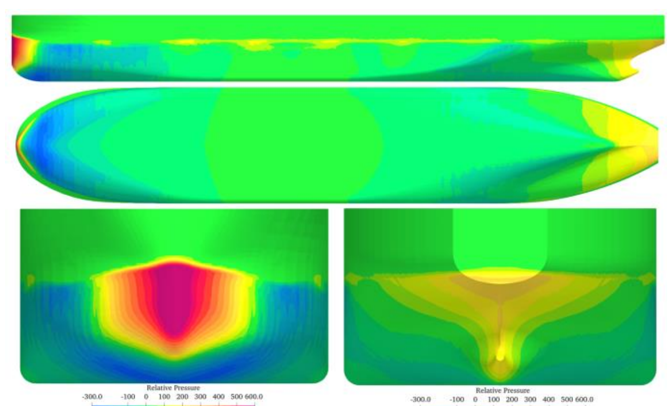

Fig. 8 Relative pressure in initial hull form surface

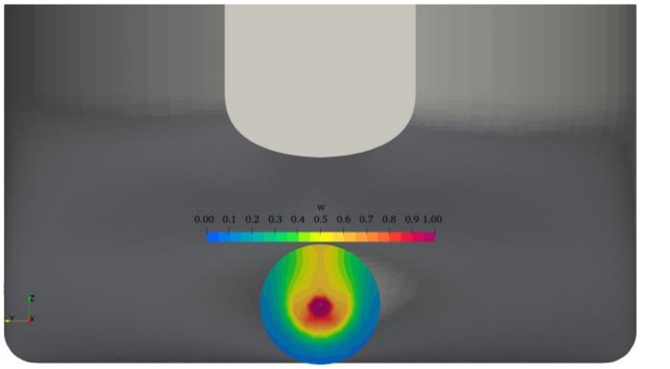

Fig. 9 Initial hull form wake in propeller disk (position: x=0.15 m, y=0 m, z=-0.31338 m)

To further verify the reliability of the CFD calculation results, a grid convergence verification was conducted. Numerical computations were performed separately using a constructed coarse-resolution grid and a high-resolution grid to examine the influence of grid resolution on the numerical results. The total number of cells in the coarse grid is 0.96 million, whereas that in the high-resolution grid is 4. 96 million. The caluculation results is shown in Table 3. According the numerical uncertainty analysis method, the $R_G = 0.401 < 1$, according to this reference (Karniadakis, 2002), the numerical results demonstrate consistent convergence. Therefore, the numerical results obtained using the selected grid resolution scheme are sufficiently reliable.

Table 3. Grid convergence

mesh	C_t-CFD (10^{-3})
Coarse	3.901
Medium	3.779
Fine	3.730

Hull Form Design Space And Optimization Condition

After completing the numerical validation against physical experiments for the initial hull, hull form optimization was subsequently carried out. First, the stern region of the hull was selected as the target optimization area, with the objectives of reducing flow separation at the hull stern and improving the inflow quality of the propeller by optimizing the stern lines of the hull. Herein, the FFD method was adopted to deform the hull stern, and the relative position between the lattice control volume and the hull is illustrated in Fig. 10. The control volume is governed by 4 control points along the longitudinal direction of the hull, 2 control points along the transverse direction, and 3 control points along the vertical direction. The lattice control volume is primarily located below the waterline (the red line in the figure denotes the hull waterline).

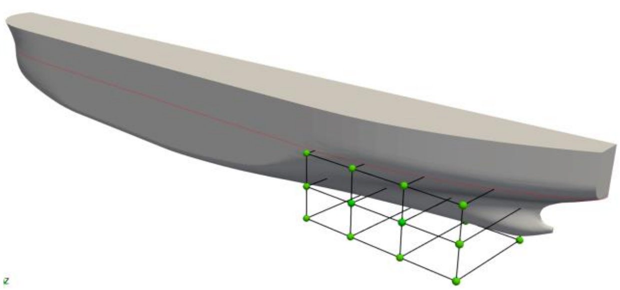

Fig. 10 The lattice for the deformation region

In this paper, two deformation parameters (denoted as x_1 and x_2) are selected to control the deformation of the hull stern. The first deformation parameter is illustrated in Fig. 11, where the red lattice control points undergo displacement (i.e., deformation along the transverse direction of the hull), thereby modifying the stern lines in the vicinity of these control points. The position of the second movable control point is presented in Fig. 12. This control point also only alters the stern lines along the transverse direction of the hull.

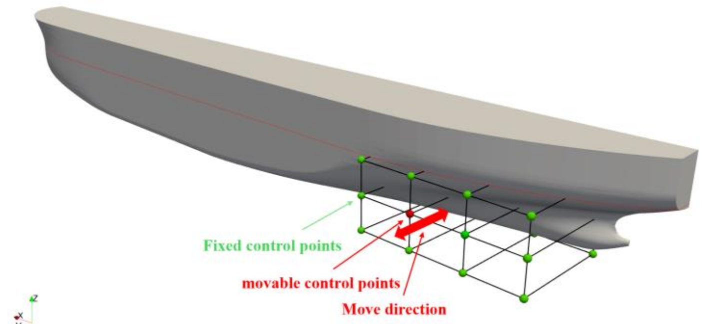

Fig. 11 The first deformation control point (the first deformation variable)

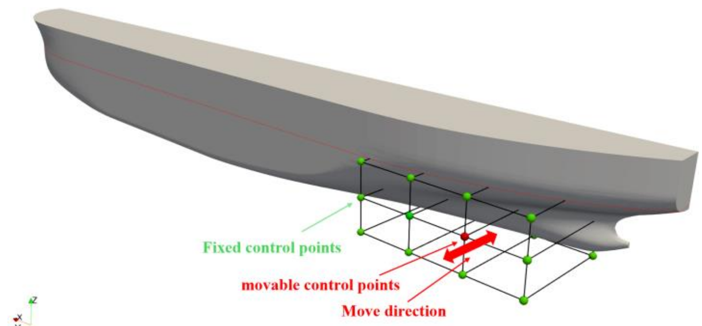

Fig. 12 The second deformation control point (the second deformation variable)

Based on the deformation constraints of the hull stern, the deformation ranges of the two parameters are determined as follows: $-0.05\ m \leq x_1 \leq 0.05\ m$, $-0.05\ m \leq x_2 \leq 0.05\ m$. The Optimal Latin Hypercube Sampling (OLHS) method is employed for sampling the deformation parameters within the design space, with a total of 20 sample points obtained. The distribution of these sample points is illustrated in Fig. 13.

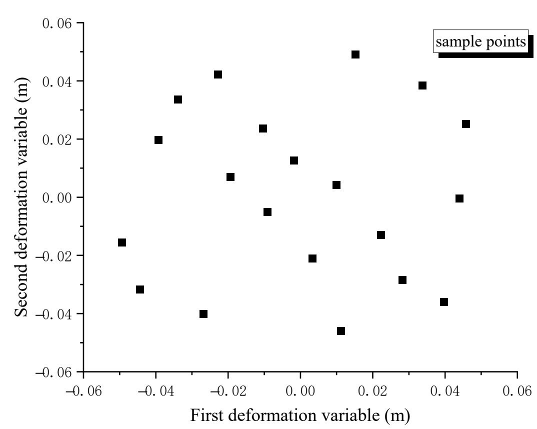

Fig. 13 The sample points distribution based on OLHS in the design space.

Mesh Morphing For Sample Hull Forms

After completion of the determination and sampling of the design space, the volume mesh of the computational domain is deformed using the developed volume mesh deformation method based on the FFD method in accordance with the sample parameters. The meshes of two randomly selected samples among the 20 are compared to observe the effect of volume mesh deformation, as illustrated in Fig. 14. It can be seen from the figure that the topological structure of the volume mesh remains unchanged before and after deformation, while the hull stern line is altered. A comparison of the hull lines before and after deformation is also presented in Fig. 15. As indicated in the figure, the hull lines remain smooth after deformation, satisfying the requirements for hull lines in actual ship construction. In the traditional hull form optimization workflow, the numerical evaluation step requires mesh generation to be performed individually for each deformed hull. For the 20 sample hull forms in this study, the total time consumed for numerical mesh generation using the traditional method is 80 minutes (with 12 CPUs operating in parallel). In contrast, the total time required by the FFD-based volume mesh deformation method is only 7 minutes when running on a single CPU. The efficiency of volume mesh generation will be further improved if parallel computing is adopted for the mesh deformation method. As can be concluded from the above analysis, the application of the volume mesh deformation method to modify the computational domain mesh and thereby achieve geometric deformation can improve the efficiency of mesh generation by more than 10 times.

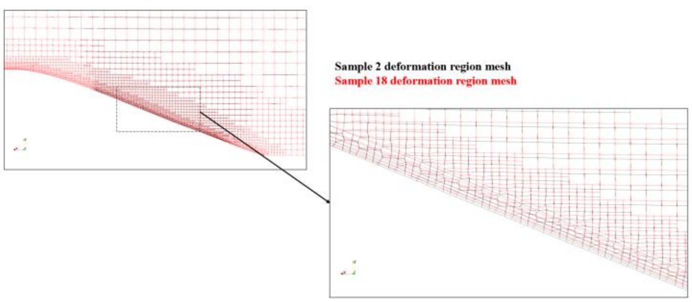

Fig. 14 Mesh morphing comparison (sample 2 and sample 18)

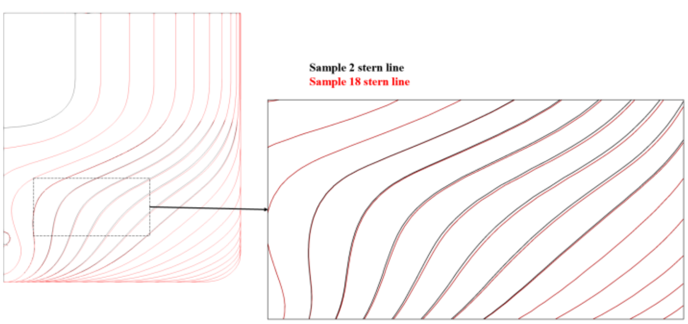

Fig. 15 Hull stern line comparison of mesh morphing (sample 2 and sample 18)

Surrogate Model And Optimization

After obtaining the numerical computational meshes corresponding to different hull forms, the two-phase incompressible flow solver embedded in OpenFOAM is employed for numerical simulations, and the resistance data of the 20 different hull forms are finally derived, as illustrated in Fig. 16.

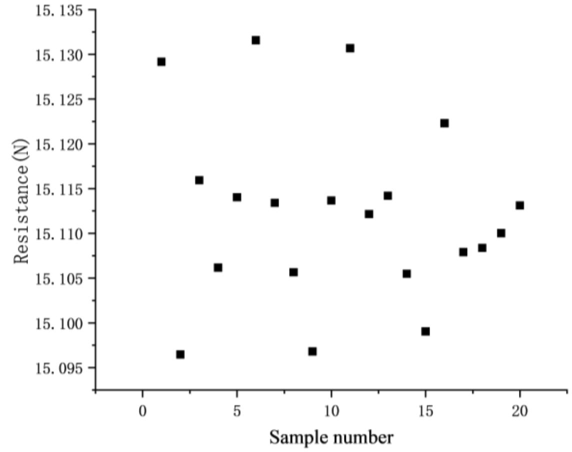

Fig. 16 The resistance distribution of 20 hull forms

A Kriging surrogate model was employed to establish the functional mapping relationship between the deformation parameters and hull resistance. Subsequently, a single-objective genetic algorithm was adopted for optimization, yielding the optimal parameters and the theoretical minimum resistance value. The iterative optimization process of the genetic algorithm is illustrated in Fig. 17, with the final optimal parameters determined as $x_1 = -0.5\ m, x_2 = -0.5\ m$. The optimized hull form was generated using the identical deformation method and subjected to numerical simulation, and its resistance value was compared with that of the initial hull form. The hull lines of the optimized hull form are presented in Fig. 18. As observed from the figure, the stern of the optimized hull form is slimmer than that of the original hull form, and the optimal parameters fall at the boundary of the design space. This indicates that a slimmer stern is more conducive to reducing hull resistance; In addition, it can decrease the wetted surface area of the hull and mitigate flow separation at the hull stern. The trend of the optimization results is consistent with basic physical laws, demonstrating the high reliability of the optimization outcomes. A comparison of the resistance between the optimized hull form and the original hull form is provided in Table 4. It can be seen from the table that the total resistance is reduced by approximately 1.47% after optimization.

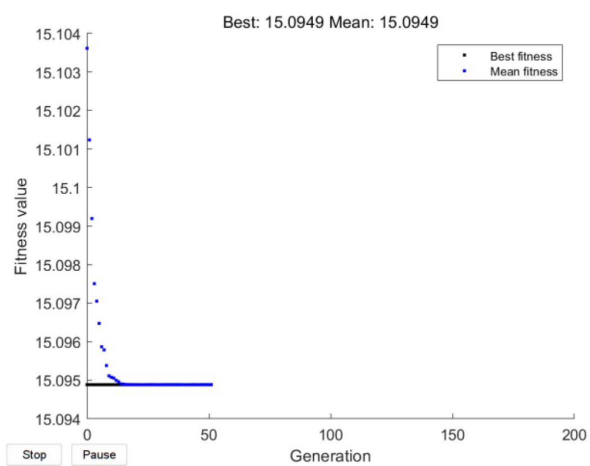

Fig. 17. Iteration of the single-objective genetic algorithm

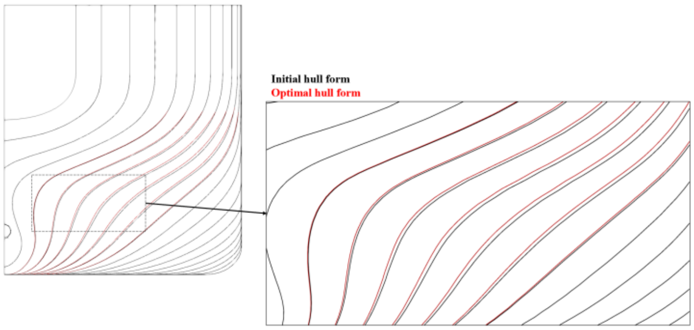

Fig. 18 Initial hull stern line and optimal hull stern line comparison

Table 4. Comparison between the initial resistance and the optimal resistance

C_t-initial (10^{-3})	C_t-optimal (10^{-3})	Optimization amplitude (%)
3.779	3.723	1.47%

Flow Field Comparison And Analysis

After obtaining the optimized hull form, a further comparative analysis was conducted on the flow fields of the optimized hull form and the original hull form. Fig. 19 presents the comparison of the propeller disk wake between the initial hull form and the optimized hull form. It can be observed from the comparison figure that the propeller disk wake of the original hull is 0.469, while that of the optimized hull form is 0.441, representing a reduction of 5.9%. The slender stern lines of the optimized hull form are conducive to improving the inflow quality of the propeller, mitigating the flow separation phenomenon at the hull stern, and thereby enhancing the propulsive efficiency of the propeller.

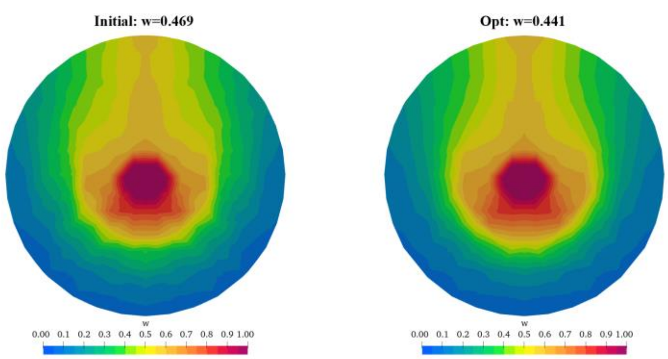

Fig. 19 Wake comparison between the initial hull form and optimal hull form in the propeller disk

Fig. 20 depicts the relative pressure distribution of the original hull form and the optimized hull form. It can be observed from the figure that the pressure distribution at the bow is basically consistent. Since the deformation magnitude of the hull stern is relatively small, there is no significant difference in the pressure distribution at the stern either. From a detailed perspective, due to the slenderized stern of the optimized hull form, the pressure gradient at the stern becomes gentler.
Fig. 21 also presents the comparison of the free surface wave patterns. It can be seen from the figure that there is almost no change in the free surface wave patterns before and after optimization. This is attributed to two aspects: on the one hand, the sailing speed is relatively low, leading to inconspicuous wave generation of the hull; on the other hand, only minor modifications were made to the underwater lines of the hull stern, which do not exert a significant impact on the free surface.

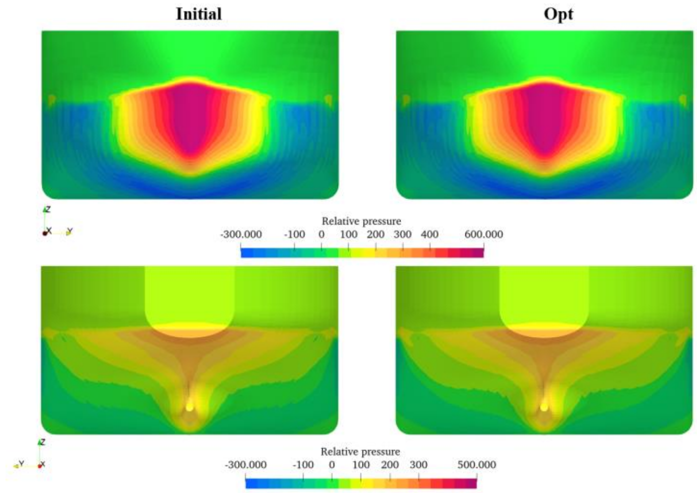

Fig. 20 Hull surface relative pressure comparison

In terms of the stern wake (Fig. 22), it can be observed that the wake fraction is the largest near the wall surface and decreases gradually as the distance from the hull surface increases. A comparison of the stern wake distributions between the original hull form and the optimized hull form reveals that their overall macro-distribution shows no significant difference. In terms of details, due to the inward contraction of the hull stern lines, the wake region also contracts inward accordingly.

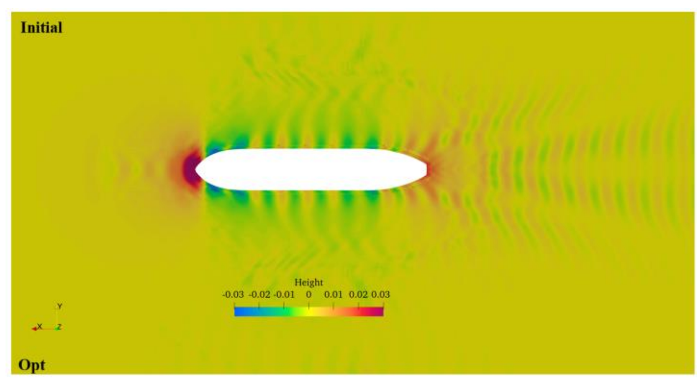

Fig. 21 Free surface comparison

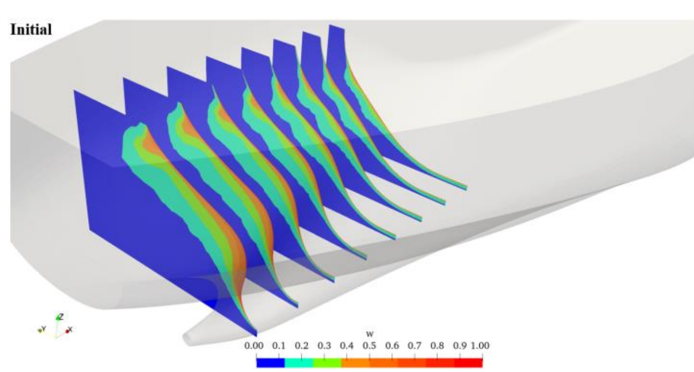

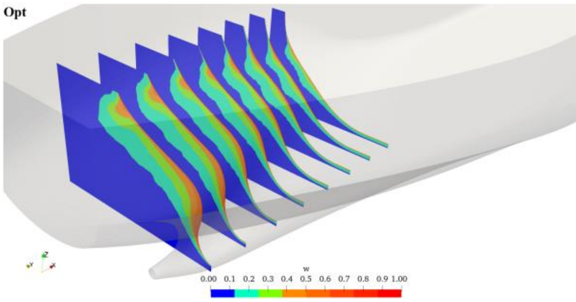

Fig. 22 Wake comparison at hull stern

CONCLUSIONS

Taking a flat merchant ship as the research object, this paper carries out the optimization of hull stern lines with the total resistance as the optimization objective. The volume mesh deformation technology based on the FFD method is adopted for the deformation of the hull stern, while maintaining the unchanged topological structure and mesh quantity of the numerical computational mesh. The application of this method improves the mesh generation efficiency by more than 10 times, thus enhancing the hull form optimization efficiency. The optimization results show that the total resistance of the optimized hull form is reduced by 1.47% through the FFD-based volume mesh deformation method, indicating that this method can not only achieve the hull optimization objective but also effectively improve the hull form optimization efficiency. In this paper, we want to show a new mesh deformation method based on FFD to conduct hull form resistance optimization, thus, we select a resistance optimization of flat merchant ship as application examples. According a application, we verify this mesh deformation method is suitable for hull form optimization. And at the same time, we only have the resistance performance of this hull, and don’t have other hydrodynamic performance experimental data. In the future, a volume mesh deformation method suitable for complex deformations can be further developed to expand the scope of hull form optimization and improve the reliability of hull form optimization.

REFERENCES

Bagheri, L., Ghassemi, H., Dehghanian, A., 2014. Optimizing the seakeeping performance of ship hull forms using genetic algorithm. TransNav: International Journal on Marine Navigation and Safety of Sea Transportation 8 (1), 49-57.

Chang, H., Liu, Z., Zhan, C., Baiwei, F., Cheng, X., Zheng, Q., 2023. Sampling method for hull form optimization based on the morphing method and its application. Ocean Engineering 281, 114715.

Costa, E., Di Paolo, B., Krassas, A., Geremia, P., Groth, C., Biancolini, M.E., 2025. Interactive Reduced Order Models for Ship Hull Design and Optimization Coupling an Open-Source CFD Tool with Advanced RBF Mesh Morphing.

Dejhalla, R., Mrša, Z., Vuković, S., 2001. Application of genetic algorithm for ship hull form optimization. International shipbuilding progress 48 (2), 117-133.

Feng, Y., el Moctar, O., Jiang, C., 2025. Hydrodynamic optimization of containership design to minimize wave-making and wave-added resistance using a weak-scatterer approach. Physics of Fluids 37 (2).

Jeong, K.-L., Jeong, S.-M., 2020. A mesh deformation method for CFD-based hull form optimization. Journal of Marine Science and Engineering 8 (6), 473.

Ji, X., Rong, Z., Wang, L., Chai, Y., Liu, X., 2025. A Novel EI-SCMC Sampling Method for Hull Form Wave-Making Resistance Optimization with Complex Constraints, ISOPE International Ocean and Polar Engineering Conference. ISOPE, pp. ISOPE-I-25-620.

Karniadakis, G.E., 2002. Quantifying Uncertainty in CFD. Journal of Fluids Engineering 124 (1), 2-3.

Kim, S.-H., Lee, C.-K., Lee, S.-M., 2021. Estimation of maneuverability of fishing vessel considering hull-form characteristics. Journal of Marine Science and Engineering 9 (6), 569.

Liu, Q., Feng, B., Liu, Z., Zhang, H., 2017. The improvement of a variance-based sensitivity analysis method and its application to a ship hull optimization model. Journal of marine science and technology 22 (4), 694-709.

Liu, X., Zhao, W., Wan, D., 2021. Linear reduced order method for design-space dimensionality reduction and flow-field learning in hull form optimization. Ocean Engineering 237, 109680.

Liu, Z., Wan, D., Zhang, X., Chen, J., Wang, S., Wang, Y., 2026. Design space nonlinear dimensionality reduction based on deep neural networks in ship hull form optimization. Ocean Engineering 348, 124112.

Miao, A., Wan, D., 2020. Hull form optimization based on an NM+ CFD integrated method for KCS. International Journal of Computational Methods 17 (10), 2050008.

Nazemian, A., Boulougouris, E., Aung, M., 2025. Hydrodynamic shape optimization of the submarine hull using the adjoint-morphing method.

Park, J.-H., Choi, J.-E., Chun, H.-H., 2015. Hull-form optimization of KSUEZMAX to enhance resistance performance. International Journal of Naval Architecture and Ocean Engineering 7 (1), 100-114.

Sederberg, T.W., Parry, S.R., 1986. Free-form deformation of solid geometric models, Proceedings of the 13th annual conference on Computer graphics and interactive techniques, pp. 151-160.

Serani, A., Diez, M., 2025. A survey on design-space dimensionality reduction methods for shape optimization. Archives of Computational Methods in Engineering, 1-28.

Villa, D., Furcas, F., Pralits, J.O., Vernengo, G., Gaggero, S., 2021. An effective mesh deformation approach for hull shape design by optimization. Journal of Marine Science and Engineering 9 (10), 1107.

Wang, L., Yuan, L., Sun, X., Qiu, W., Liu, X., 2025. An Improved Three-dimensional Shifting Method for Hull Form Drag Optimization, ISOPE International Ocean and Polar Engineering Conference. ISOPE, pp. ISOPE-I-25-622.

Wang, P., Feng, Y., Chen, Z., Dai, Y., 2023. Study of a hull form optimization system based on a Gaussian process regression algorithm and an adaptive sampling strategy, Part II: Multi-objective optimization. Ocean Engineering 286, 115501.

Zhang, Y., Ma, N., Gu, X., Shi, Q., 2023. A Dimensionality Reduction Method Based on Principal Component Analysis for Ship Hull Form Optimization, ISOPE International Ocean and Polar Engineering Conference. ISOPE, pp. ISOPE-I-23-519.